1   **Asymmetric peptidoglycan editing generates the curvature of predatory**

2   **bacteria, optimizing invasion and replication within a spherical prey**

3   **niche**

4   Emma J. Banks[1], Mauricio Valdivia-Delgado[2], Jacob Biboy[3], Amber Wilson[2], Ian T. Cadby[2],

5   Waldemar Vollmer[3], Carey Lambert[1], Andrew L. Lovering[2]*, R. Elizabeth Sockett[1]*

6   *corresponding authors:

7   liz.sockett@nottingham.ac.uk +44 (07851775626)

8   a.lovering@bham.ac.uk +44 (07933950457)

9

10 Author affiliations:

11 [1]Medical School, School of Life Sciences, University of Nottingham, Queen's Medical

12 Centre, Nottingham, NG7 2UH, UK

13 [2]Institute for Microbiology and Infection, School of Biosciences, University of Birmingham,

14 Birmingham, B15 2TT, UK

15 [3]Center for Bacterial Cell Biology, Biosciences Institute, Newcastle University, Newcastle

16 upon Tyne, NE2 4AX, UK

17

18

19

20

21

22

23

24   **Abstract**

25   The vibrioid predatory bacterium *Bdellovibrio bacteriovorus* secretes prey wall-

26   modifying enzymes to invade and replicate within the periplasm of Gram-negative prey

27   bacteria. Studying self-modification of predator wall peptidoglycan during predation,

28   we discover that Bd1075 generates self-wall curvature by exerting LD-

29   carboxypeptidase activity in the vibrioid *B. bacteriovorus* strain HD100 as it grows

30   inside spherical prey. Bd1075 localizes to the outer curved face of *B. bacteriovorus*, in

31   contrast to most known shape-determinants. Asymmetric protein localization is

32   determined by the novel function of a nuclear transport factor 2-like (NTF2) domain at

33   the protein C-terminus. The solved structure of Bd1075 is monomeric, with key

34   differences to other LD-carboxypeptidases. Rod-shaped Δ*bd1075* mutants invade

35   prey more slowly than curved wild-type predators, and stretch and deform the invaded

36   prey cell from within. Vibrioid morphology increases the evolutionary fitness of wild

37   predatory bacteria, facilitating efficient prey invasion and intracellular growth of curved

38   predators inside a spherical prey niche.

39

40

41

42

43

44

45

46

47   **Introduction**

48   *Bdellovibrio bacteriovorus* HD100 is a small, vibrioid-shaped predatory bacterium

49   which invades and then replicates within the periplasm of Gram-negative prey

50   bacteria, forming a spherical structure called a prey bdelloplast[1]. *B. bacteriovorus* has

51   a broad prey range which includes multidrug-resistant pathogens with variable outer

52   membrane and cell wall chemistries, and occurrence of genetic resistance to *B.*

53   *bacteriovorus* has never been observed in prey bacteria[2, 3]. Predatory *B. bacteriovorus*

54   can also successfully clear pathogen infections within a range of *in vivo* animal

55   models[4, 5, 6] and therefore has considerable and growing potential as a novel

56   antimicrobial therapeutic.

57   The predation process is critically dependent upon the modification of both predator

58   and prey peptidoglycan (PG) cell walls to facilitate the dual bacterial encounter. PG

59   forms a complex macromolecular structure called a sacculus which surrounds the

60   cytoplasmic membrane of nearly all bacteria, maintaining cell shape and providing

61   protection against lysis due to osmotic pressure fluctuations and large extracellular

62   toxins[7]. Bacterial growth, cell division, and – importantly in this study – predation, occur

63   through PG remodeling which involves a repertoire of predator-secreted modifying

64   enzymes[8, 9, 10, 11].

65   The predatory lifecycle of *B. bacteriovorus* begins with attack-phase cells which swim[12]

66   or glide[13] to encounter prey, then recognize and attach to the prey outer membrane.

67   An entry porthole in the prey cell wall is created, through which the predator traverses

68   to enter the inner periplasmic compartment[10]. Concurrently, two predator DD-

69   endopeptidases are secreted into prey, cleaving cross-links between prey PG peptide

70   chains to sculpt rod-shaped prey cells into spherical bdelloplasts[8]. This also reduces

71   the frequency of sequential predator invasions, thus conferring exclusivity to the first-

72   entering predator[8]. The porthole in the wall and outer membrane is then re-sealed and

73   the predator secretes hydrolytic enzymes including nucleases and proteases into the

74   cytoplasm of the now-dead host, taking up the nutrient-rich degradative products[14, 15].

75   Prey-derived and *de novo*-synthesized nucleotides are incorporated into the

76   replicating genome copies of the predator, which grows as an elongating multi-

77   nucleoid filament inside the rounded but intact prey until exhaustion of prey nutrients[16].

78   Synchronous septation of the predator filament yields progeny cells which secrete

79   targeted PG hydrolytic enzymes to lyse the prey host and re-initiate the predatory

80   cycle[11].

81   PG hydrolases have an additional role generally in the determination of cell shape[17],

82   which has been particularly studied in the non-predatory, ε-proteobacteria

83   *Helicobacter pylori*[18, 19, 20] and *Campylobacter jejuni*[21, 22, 23], in whom multiple PG

84   hydrolases collectively generate helical morphology. In contrast, bacterial vibrioid

85   morphology is generally determined by non-enzymatic cyto- or periskeletal proteins

86   (well-studied in *Caulobacter crescentus*[24, 25] and *Vibrio cholerae*[26]).

87   Despite the characterization of predator enzymes which modify the prey PG, there

88   have been very few studies concerning the cell wall PG architecture or vibrioid cell

89   shape of predatory bacteria. Here, we investigate the mechanism by which a curved,

90   vibrioid predator is generated and ask whether there are evolutionary and functional

91   connections between predator cell morphology and an efficient predatory lifestyle.

92   We identify and characterize the first predatory cell shape-determinant: Bd1075, which

93   is targeted to the outer convex cell face by its C-terminal nuclear transport factor 2-

94   like (NTF2) domain, where it exerts localized LD-carboxypeptidase (LD-CPase)

95   activity upon the *B. bacteriovorus* PG wall to generate curvature and the classical

96   vibrio shape. The Bd1075 protein has some novel features in comparison to other LD-

97   CPases, being monomeric with a C-terminal extension to the NTF2 domain binding

98   pocket. We discover that rod-shaped Δ*bd1075* mutant predators invade prey more

99   slowly than the curved wild-type and stretch and deform the prey cell bdelloplast while

100   growing within, unlike the curved wild-type. We further note that there is dynamic

101   adaptation to the spherical prey niche; both curved wild-type and rod-shaped Δ*bd1075*

102   mutant predators temporarily adopt a curve while growing inside the spherical prey

103   bdelloplast, however only wild-type predators exit prey with a permanent vibrioid

104   shape.

105   Our findings suggest that the evolution of a vibrioid cell shape confers two fitness

106   advantages to *B. bacteriovorus* predators: rapid prey entry and optimal replication

107   within a spherical intra-bacterial niche. This discovery also implies a possible scenario

108   in which cell curvature may first be "templated" by predatory growth inside a

109   spherically-shaped structure, then sensed and permanently "fixed" by PG shape-

110   determining enzymes.

111

112

113

114

115

116

117

118 **Results**

119 **Bd1075 generates the curvature of *B. bacteriovorus* predators**

120 The monocistronic *bd1075* gene of vibrioid-shaped *B. bacteriovorus* Type strain

121 HD100 encodes a 329 amino acid hypothetical protein with a predicted N-terminal sec

122 signal peptide[27], suggestive of protein translocation into the periplasm or secretion

123 from the cell (Supplementary Fig. 1). Bd1075 shares limited homology with Csd6

124 (identity: 24%, similarity: 38%) and Pgp2 (identity: 25%, similarity: 40%) which are

125 dimeric proteins important for the generation of helical cell shape in *H. pylori*[18, 28] and

126 *C. jejuni*[21], respectively. These comparisons led us to hypothesize that Bd1075 could

127 fulfill a role in the shape-determination of vibrioid predator *B. bacteriovorus*.

128 Reverse-transcriptase PCR (RT-PCR) revealed that *bd1075* is constitutively

129 transcribed throughout the predatory cycle, suggesting that the protein may have a

130 role in *B. bacteriovorus* rather than a secreted predatory function (Supplementary Fig.

131 2).

132 A markerless deletion of *bd1075* in the curved *B. bacteriovorus* Type strain HD100

133 could still be cultured predatorily (phenotype differences further detailed later) but

134 Δ*bd1075* mutant cells had a distinct straight rod-shaped morphology unlike the curved

135 wild-type HD100 parent strain (Fig. 1a-b). Wild-type mean curvature was significantly

136 higher than the Δ*bd1075* mutant (0.61 A.U. ± SD 0.33 *versus* 0.17 A.U. ± SD 0.22,

137 respectively, p<0.0001; Fig. 1c). Plasmid-based complementation of Δ*bd1075* with the

138 wild-type *bd1075*$_{HD100}$ gene increased curvature relative to the Δ*bd1075* mutant (Fig.

139 1c). These results indicate that Bd1075 has a role in generating the curvature of *B.*

140 *bacteriovorus*.

141

A lab-evolved predator strain that cannot generate cell curvature

142

143 The straight rod morphology of $\Delta bd1075$ resembles the long-cultured laboratory strain

144 *B. bacteriovorus* 109J which was isolated in the 1960s and is the only reported non-

145 vibrioid strain of *B. bacteriovorus*[1]. As *bd1075* is conserved in all *B. bacteriovorus*

146 strains including 109J and appears to be a curvature-determinant, we queried why

147 strain 109J is non-vibrioid. Despite otherwise 100% sequence identity with

148 *bd1075*$_{HD100}$, *bd1075*$_{109J}$ contains an in-frame N-terminal truncation of 57 amino acids

149 (Pro-18 to Tyr-74) (Supplementary Fig. 3a-c). RT-PCR confirmed that *bd1075*$_{109J}$ is

150 expressed in attack-phase cells and that the RNA transcript contains the predicted

151 truncation (Supplementary Fig 3d). To test whether the N-terminal truncation may

152 render the translated protein non-functional in curvature-determination, we cross-

153 expressed *bd1075*$_{109J}$ in the HD100 $\Delta bd1075$ mutant and this did not complement

154 curvature (Supplementary Fig. 4). In contrast, cross-expression of *bd1075*$_{HD100}$ in wild-

155 type 109J significantly increased the curvature of strain 109J (0.34 A.U. ± SD 0.26

156 *versus* 0.22 A.U. ± SD 0.21, respectively, $p<0.0001$; Supplementary Fig 4)

157 These results show that Bd1075 is the curvature-determinant of vibrioid *B.*

158 *bacteriovorus* strains, and that an inactivating mutation within the gene resulted in the

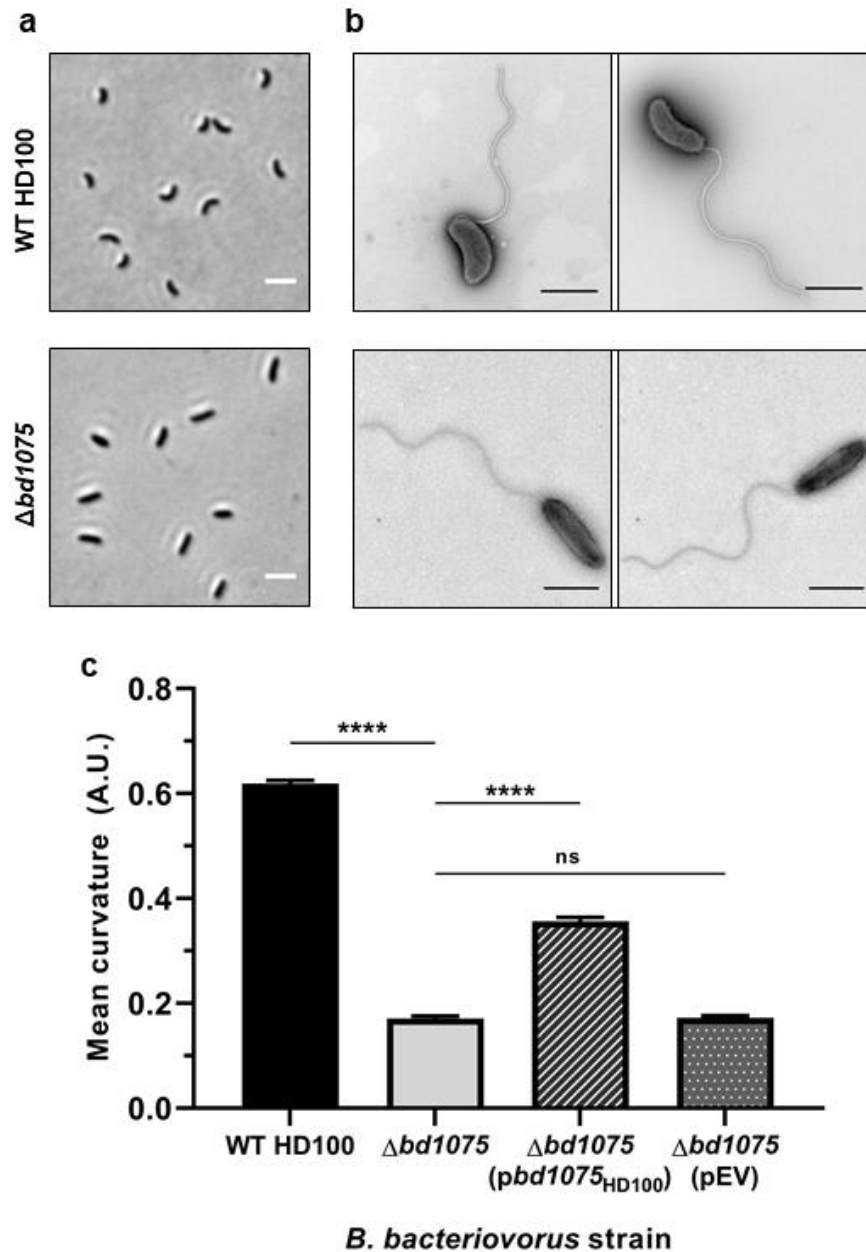159 lab-evolved strain 109J which is unable to generate cell curvature.

Fig. 1 Bd1075 generates the curvature of *B. bacteriovorus* HD100 predator cells.

a Phase-contrast images of attack-phase *B. bacteriovorus* cells showing the curvature of wild-type (WT) HD100 cells in comparison to non-vibrioid Δ*bd1075* cells. Images are representative of cells from at least 5 biological repeats. Scale bars = 2 μm. **b** Transmission electron micrographs of WT HD100 and Δ*bd1075* cells stained with 0.5% uranyl acetate. Scale bars = 1 μm. Images are representative of 3 biological repeats. **c** Curvature measurements of *B. bacteriovorus* attack-phase cells. n = 1920-2503 cells per strain from 3 biological repeats. Error bars represent standard error of the mean. ns: non-significant ($p > 0.05$), ****: $p < 0.0001$; Kruskal-Wallis test. Frequency distributions are included in Supplementary Fig. 5a.

160   **Rod-shaped Δ*bd1075* predators invade prey more slowly than the curved wild-**

161   **type**

162   As cell morphology can be phenotypically important in other bacteria, we asked

163   whether the curved shape of *B. bacteriovorus* could be advantageous to the bacterial

164   predator during its unique intraperiplasmic lifecycle. Comparison of the gross

165   predation efficiency of wild-type and Δ*bd1075* predators upon *E. coli* prey in either

166   liquid culture, or on pre-grown *E. coli* biofilms, did not reveal a significant difference

167   (Supplementary Fig. 6 and Supplementary Fig. 7). However, these are laboratory

168   conditions with readily-available prey and in which multiple important factors required

169   to locate and navigate towards prey (e.g. predator chemotaxis and locomotion) are

170   operational in bringing predators close to the prey surface.

171   We considered that predator morphology may fulfill an important role at the interface

172   of single predator-prey encounters and therefore studied predation more closely at the

173   single-cell level using time-lapse microscopy to visualize individual predatory invasion

174   events. *B. bacteriovorus* HD100 wild-type or Δ*bd1075* strains were mixed with *E. coli*

175   S17-1 and placed under a microscope which captured images of specific fields of view

176   every 1 min until the majority of *E. coli* prey had been invaded. Hypothesizing that

177   curvature may affect the invasion of *B. bacteriovorus* into prey, we measured two

178   parameters: prey attachment time and prey entry time (Fig. 2a). Duration of prey

179   attachment did not significantly differ (p = 0.46) between the wild-type (29.3 min ± SD

180   5.0) and Δ*bd1075* (29.6 min ± SD 4.8) (Fig. 2b), however there was a significant

181   difference (p<0.0001) between the rates at which wild-type and Δ*bd1075* entered prey:

182   4.3 min ± SD 0.9 *versus* 6.1 min ± SD 1.7, respectively (Fig. 2c). Moreover, the longest

183   wild-type entry was a single 7 min invasion, whereas 35.6% of Δ*bd1075* entry

184   invasions were ≥ 7 min, with the longest invasion lasting 14 min.

185   These data indicate that *B. bacteriovorus* vibrioid morphology facilitates the traversal

186   of predators across the prey cell envelope into the intraperiplasmic compartment of

187   the rounded prey cell.
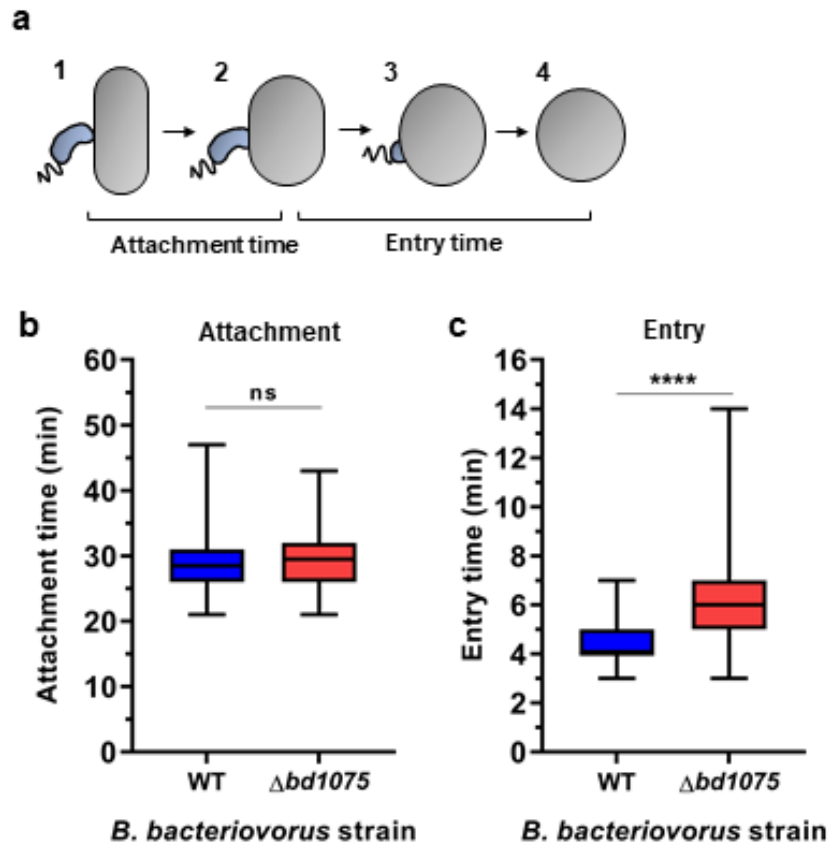
188

189

190

191

192

193

194

195

196

197

Fig. 2 Prey attachment and entry times of *B. bacteriovorus* wild-type and Δ*bd1075*.

a Schematic to illustrate the measurement of attachment and entry times. Attachment time: number of frames (1 frame = 1 min) between initial predator attachment to prey and the first sign of predator entry into prey (stages 1-2). Entry time: number of frames between the first sign of predator entry and the predator residing completely inside the prey bdelloplast (stages 2-4). **b** Duration of attachment to and **c** entry into *E. coli* S17-1 prey by *B. bacteriovorus* HD100 wild-type (WT) and Δ*bd1075*, measured by time-lapse microscopy. n = 90 cells in total from 3 biological repeats. Box: 25th to 75th percentiles; whiskers: range min-max; box line: median; ns: non-significant (p>0.05); ****: p<0.0001; Mann-Whitney test.

198

199

200

201

202 **Prey bdelloplasts are stretched and deformed by replicating, non-curved**

203 **predators**

204 Having observed that the non-vibrioid Δ*bd1075* mutant was slower to enter the prey

205 periplasm than the curved wild-type, we next investigated the growth and replication

206 of Δ*bd1075* within prey. During prey invasion, *B. bacteriovorus* secretes two DD-

207 endopeptidases, Bd0816 and Bd3459, into the prey periplasm which hydrolyze the

208 peptide bonds connecting chains of polysaccharide backbone[8]. The prey PG wall

209 becomes more malleable and the cell rounds up into a spherical bdelloplast.

210 We hypothesized that growth of the straight rod-shaped Δ*bd1075* within spherical

211 bdelloplasts may be deleterious to the predatory niche, whereas curved wild-type cells

212 may better "fit" into the curvature of the bdelloplast during growth and elongation. A C-

213 terminal mCerulean3 fusion to the continuously-expressed cytoplasmic protein

214 Bd0064[6, 29] was introduced via single-crossover recombination into both wild-type

215 HD100 and Δ*bd1075* to label the predator cytoplasm blue and allow visualization of *B.*

216 *bacteriovorus* within prey. Fluorescent *B. bacteriovorus* strains were mixed with *E. coli*

217 S17-1 pZMR100 and observed throughout the predatory cycle. Wild-type predators

218 elongated as tightly curved filaments inside bdelloplasts (Fig. 3a), however the rod-

219 shaped Δ*bd1075* mutant - despite becoming more curved by the spherical bdelloplast

220 environment over time (Fig. 3b) - elongated as a less tightly curved filament and then

221 septated to give rod-shaped, non-vibrioid progeny cells (Fig. 3a). Strikingly, a sub-set

222 of Δ*bd1075* predator cells appeared to stretch and deform the usually spherical prey

223 bdelloplasts during intra-bacterial growth (Fig. 3c).

224 Measuring the morphology of bdelloplasts containing a single *B. bacteriovorus*

225 predator between 1 h and 2.5 h after predator-prey mixing showed that from 1 h - 2 h,

226   the shape of prey bdelloplasts did not obviously differ between the two strains.

227   However, at 2.5 h when *B. bacteriovorus* cells are nearing maximal growth, the

228   morphology of prey bdelloplasts became markedly different. The area of each

229   bdelloplast containing a $\Delta bd1075$ mutant predator (1.87 μm^2 ± SD 0.57) was

230   significantly higher than bdelloplasts containing wild-type predators (1.69 μm^2 ± SD

231   0.32, p<0.01; Fig. 3d) and the circularity was significantly lower ($\Delta bd1075$: 0.98 A.U.

232   ± SD 0.04; wild-type: 0.99 A.U. ± SD 0.01, p<0.05; Fig. 3e). Bdelloplasts containing

233    $\Delta bd1075$ predators were also significantly longer (1.65 μm ± SD 0.36, p<0.01; Fig. 3f)

234   than those containing curved wild-type predators (1.54 μm ± SD 0.18) but the width

235   did not significantly differ ($\Delta bd1075$: 1.38 μm ± SD 0.13; wild-type: 1.35 μm ± SD 0.09,

236   p>0.05; Fig. 3g), consistent with the visual appearance of "stretched" bdelloplasts.

237   Collectively, these findings show that curved *B. bacteriovorus* wild-type cells have an

238   "optimal fit" into the curvature of the bdelloplast, whereas the shape of rod-shaped

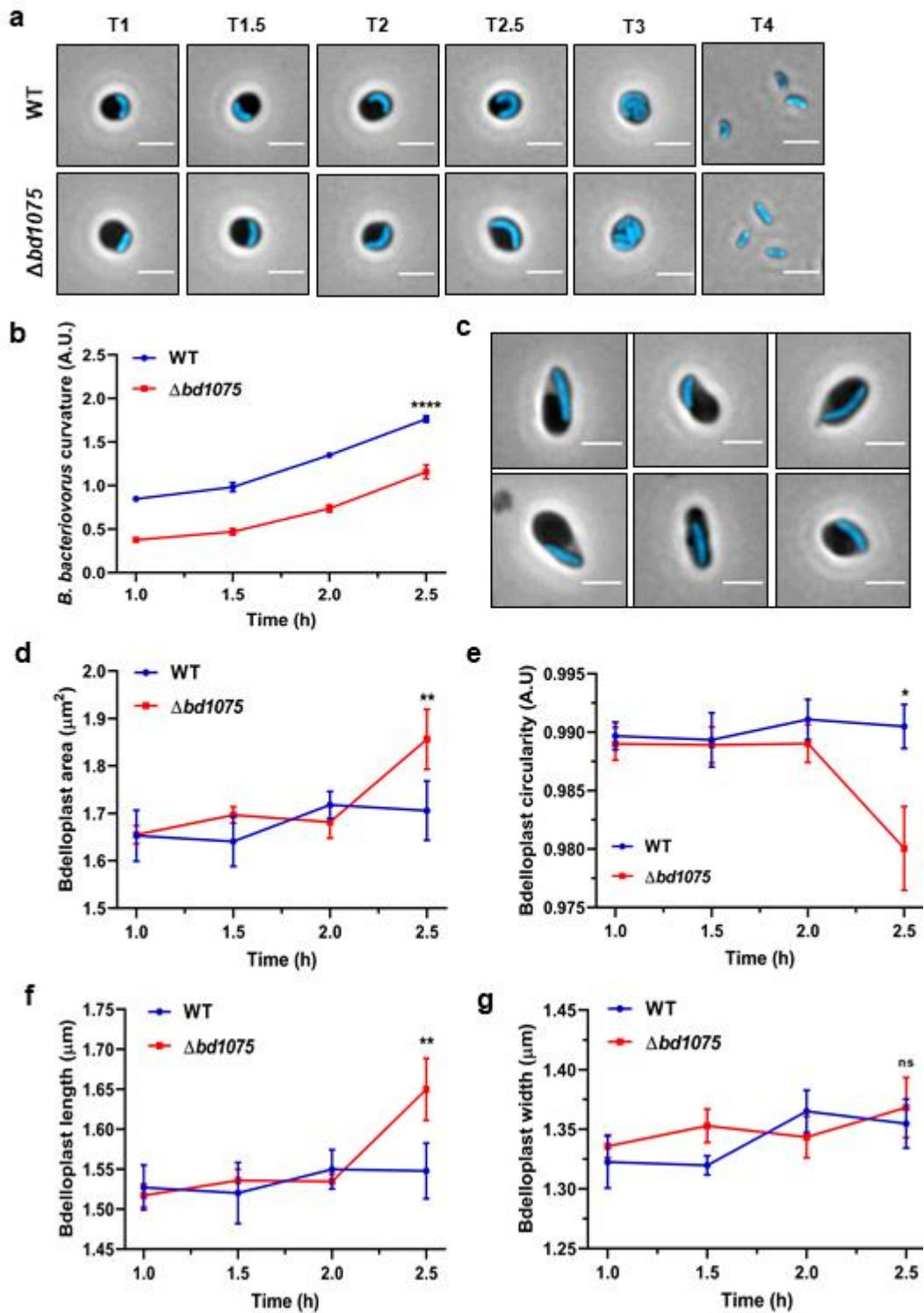239   predators can result in severe deformation of the spherical prey niche.

Fig. 3 Intra-bacterial growth and bdelloplast topology effects of *B. bacteriovorus* strains.

a Growth of *B. bacteriovorus* wild-type (WT) and Δ*bd1075* strains inside *E. coli* S17-1 pZMR100 prey bdelloplasts. *B. bacteriovorus* strains express the cytoplasmic fusion protein Bd0064-mCerulean3 to allow visualization of intraperiplasmic predator cells. T = hours elapsed since predators and prey were mixed. Scale bars = 2 μm. Images are representatives of cells from 3 biological repeats. **b**

Curvature of *B. bacteriovorus* WT and Δ*bd1075* strains during predation upon *E. coli* S17-1 pZMR100 as depicted in (**a**). n = 134-250 cells per strain and per timepoint from 3 biological repeats. Error bars represent standard error of the mean. ****: p<0.0001; Mann-Whitney test. **c** Examples of Δ*bd1075* cells which appear to stretch and deform the *E. coli* prey bdelloplast at T = 2.5 h during 3 repeats of predatory timecourses as shown in (**a**). Scale bars = 2 µm. **d** Area, **e** circularity, **f** length and **g** width of *E. coli* prey bdelloplasts during predation by WT or Δ*bd1075* predators. n = 134-250 cells per strain and per timepoint from 3 biological repeats. Error bars represent standard error of the mean. ns: non-significant (p>0.05); **: p<0.01, *: p<0.05; Mann-Whitney test.

240

241

242

243

244

245

246

247

248

249

250

251

252

253

254

255

256

257

258

259

260 **Bd1075 demonstrates LD-carboxypeptidase activity on PG sacculi *in vivo* and**

261 ***in vitro***

262 Bd1075 contains a predicted LD-transpeptidase (LDT) catalytic domain

263 (Supplementary Fig. 1c-d), however the LDT domains of related proteins Csd6 and

264 Pgp2 function instead as LD-carboxypeptidases (LD-CPases) which remove the

265 terminal D-alanine from a PG tetrapeptide (consisting of L-Ala, D-Glu, *meso*-Dap, and

266 D-Ala) to generate a tripeptide (consisting of L-Ala, D-Glu, and *meso*-Dap)[30]. This

267 highlighted the need to verify the catalytic activity (if any) of Bd1075. PG sacculi were

268 therefore purified from *B. bacteriovorus* strains and analyzed by HPLC to determine

269 their muropeptide composition and any changes to it caused by Bd1075.

270 In contrast to curved wild-type HD100 sacculi, rod-shaped Δ*bd1075* sacculi contained

271 a greater proportion of monomeric tetrapeptides (23.7% ± 0.8%) and cross-linked

272 tetratetrapeptides (33.2% ± 0.7%) compared to the wild-type (9.6% ± 0.8% and 18.6%

273 ± 0.6%, respectively), and a complete absence of monomeric tripeptides and dimeric

274 tetratripeptides (Fig. 4a-b and Table 1). This difference suggests that Bd1075 could

275 cleave the C-terminal D-alanine of tetrapeptides to produce tripeptides which

276 terminate with *meso*-Dap. The complemented strain Δ*bd1075* (p*bd1075*HD100)

277 contained no monomeric tetrapeptides, 14.8% ± 1.2% tripeptides and 7.2% ± 0.5%

278 dipeptides. These data suggest that re-introduction of the wild-type *bd1075*HD100 gene

279 resulted in over-complementation beyond wild-type as all monomeric tetrapeptides

280 have been cleaved to tripeptides, with some subsequently converted to dipeptides

281 (Fig. 4c and Table 1).

282 In comparison, the muropeptide profile of strain Δ*bd1075* (p*bd1075*109J), in which

283 curvature was not complemented (Supplementary Fig. 4), did not differ from Δ*bd1075*,

284   further confirming the non-functionality of truncated $Bd1075_{109J}$ as an LD-CPase

285   (Supplementary Fig. 8a and Supplementary Table 1).

286   Wild-type 109J had a very similar muropeptide profile to the $\Delta bd1075$ mutant - a

287   complete absence of tripeptides and tetratripeptides and a high proportion of

288   monomeric tetrapeptides (28.0% ± 4.3%) and dimeric tetratetrapeptides (33.8% ±

289   1.1%) (Supplementary Fig. 8b and Supplementary Table 1). Finally, the cross-

290   complementation strain 109J (p$bd1075_{HD100}$), with an increased mean curvature

291   compared to the lab-cultured wild-type strain 109J (Supplementary Fig. 4), contained

292   a higher proportion of monomeric tripeptides (18.7% ± 3.0%) and dimeric

293   tetratripeptides (26.2% ± 0.6%), and a reduction in monomeric tetrapeptides and

294   dimeric tetratetrapeptides (3.0% ± 0.8% and 8.8% ± 0.8%, respectively)

295   (Supplementary Fig. 8c and Supplementary Table 1). This demonstrates that cross-

296   expression of $bd1075_{HD100}$ in wild-type 109J resulted in enzymatic conversion of

297   tetrapeptides to tripeptides and increased the curvature of this normally non-vibrioid

298   strain.

299   To further validate the LD-CPase activity of Bd1075, an N-terminally His-tagged copy

300   of $bd1075_{HD100}$ was expressed in *E. coli* BL21 and purified to near homogeneity by Ni-

301   NTA affinity chromatography and size-exclusion chromatography. The muropeptide

302   profile of *B. bacteriovorus* HD100 $\Delta bd1075$ sacculi incubated with purified Bd1075

303   enzyme revealed a complete conversion of both monomeric tetrapeptides to

304   tripeptides and dimeric tetratetrapeptides to tetratripeptides (Fig. 4e). Bd1075 had

305   identical enzymatic activity on wild-type 109J straight rod sacculi and upon sacculi of

306   wild-type *E. coli* BW25113, showing that the enzyme can act on PG from different

307   bacterial strains and species (Supplementary Fig. 9b-c).

308   These muropeptide data determine that Bd1075 has LD-CPase activity on PG both *in*

309   *vivo* and *in vitro*, removing C-terminal D-alanine residues linked to the L-center of

310   *meso*-Dap to convert tetrapeptides to tripeptides.
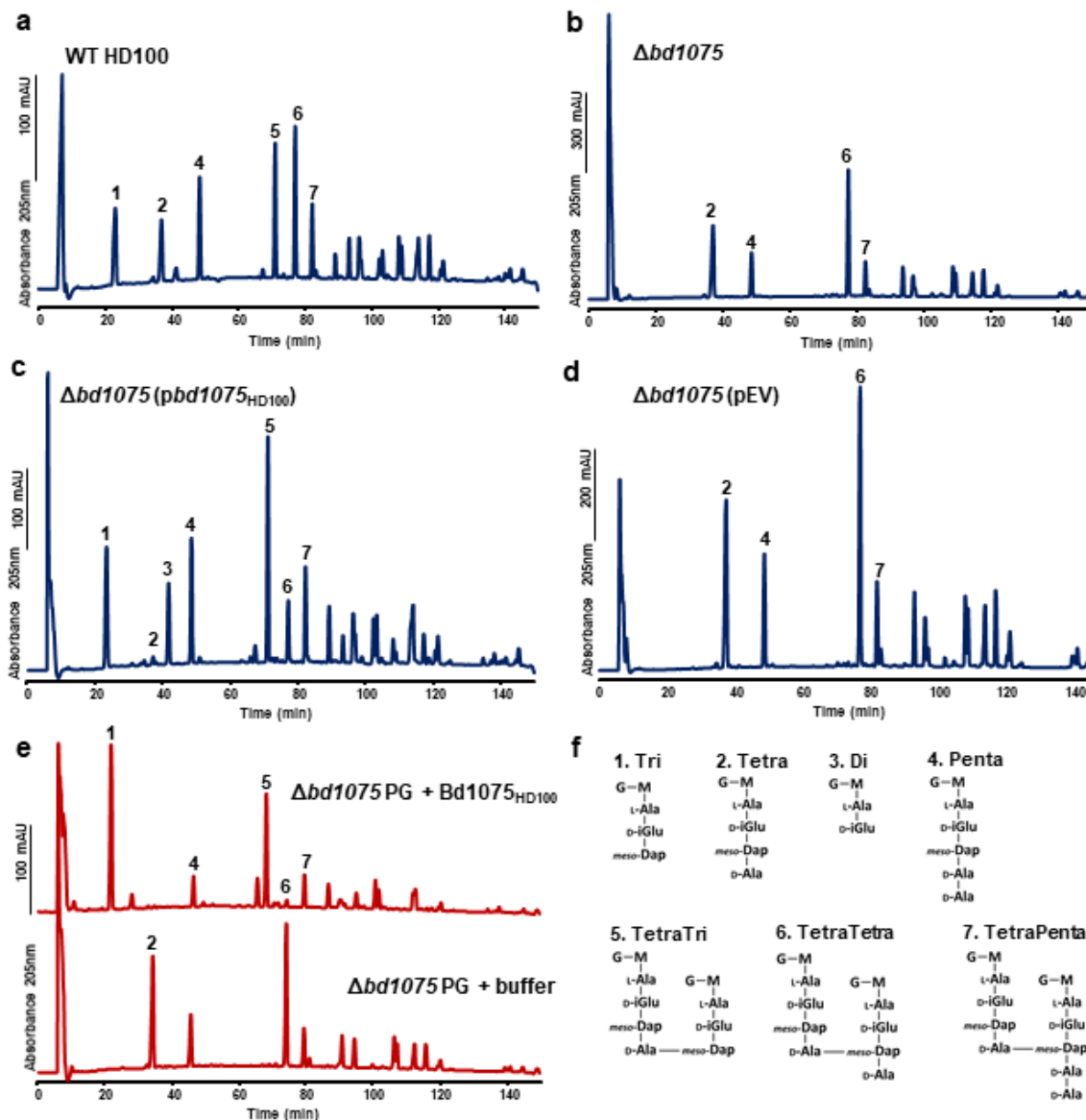
311

312

313

314

315

Fig. 4 Muropeptide composition of *B. bacteriovorus* HD100

a-d HPLC elution profiles of reduced muropeptides released from peptidoglycan sacculi isolated from attack-phase *B. bacteriovorus* HD100 cells. **a** Wild-type (WT) HD100, **b** Δ*bd1075*, **c** Δ*bd1075* (p*bd1075*HD100) - *bd1075*HD100 expressed in Δ*bd1075*, and **d** Δ*bd1075* (pEV) - empty vector control in Δ*bd1075*. Representative chromatograms of 2 biological repeats are shown. **e** HPLC muropeptide elution profiles of Δ*bd1075* sacculi treated with either purified Bd1075HD100 enzyme (above) or buffer control (below). Data are from 1 biological repeat. **f** Structural schematics of the seven primary muropeptide fractions. Numbers correspond to those above peaks in (**a-e**). G: *N*-acetylglucosamine, M: *N*-acetylmuramitol, L-Ala: L-alanine, D-Glu: D-glutamic acid, *meso*-Dap: *meso*-diaminopimelic

acid, D-Ala: D-alanine. Minor peaks are annotated in Supplementary Fig. 10 (for **a-d**) or Supplementary Fig. 9a (for **e**).

316

317

318

319

320

321

322

323

324

325

326

327

328

329

330

331

332

333

Table 1. Quantification of muropeptides released from *B. bacteriovorus* HD100 sacculi.

Values represent the relative percentage area of each muropeptide peak in **Fig. 4.** Numbers with an asterisk differ from WT HD100 by more than 30% and values that are additionally emboldened differ by more than 50%.

Muropeptide	Relative peak area (%)[1] in *B. bacteriovorus* strain			
	WT HD100	Δ*bd1075*	Δ*bd1075* (p*bd1075*HD100)	Δ*bd1075* (pEV)
Monomers				
Tri	14.4 ± 1.0	n.d.*[2]	14.8 ± 1.2	n.d.*
Tetra	9.6 ± 0.8	**23.7 ± 0.8***	**0.6 ± 0.9***	**23.1 ± 2.7***
Di	2.1 ± 0.1	n.d.*	7.2 ± 0.5*	n.d.*
Penta	12.8 ± 2.5	11.9 ± 3.6	12.2 ± 4.2	14.8 ± 0.0
Monomer anhydroMurNAc	2.2 ± 3.0	2.3 ± 3.2	2.6 ± 3.7	2.5 ± 3.6
Monomers (Total)	38.9 ± 0.5	35.6 ± 4.3	34.9 ± 2.6	37.8 ± 2.6
Dimers				
TetraTri	14.9 ± 0.7	**0.5 ± 0.7***	**26.4 ± 1.5***	n.d.*
TetraTetra	18.6 ± 0.6	**33.2 ± 0.7***	**7.8 ± 1.4***	**29.6 ± 4.7***
TetraPenta	12.2 ± 1.0	12.5 ± 0.3	14.7 ± 2.9	13.1 ± 0.2
Dimer anhydroMurNAc	17.3 ± 0.8	16.4 ± 0.6	20.5 ± 4.4	17.0 ± 0.3
Dimers (total)	45.6 ± 2.3	46.1 ± 0.6	48.9 ± 2.9	42.7 ± 4.5
Trimers				
TetraTetraTri	1.6 ± 0.4	n.d.*	3.8 ± 0.2*	n.d.*
TetraTetraTetra	6.9 ± 0.5	**11.2 ± 0.8***	4.9 ± 1.0	**10.6 ± 2.2***
TetraTetraPenta	6.9 ± 3.6	7.1 ± 3.2	7.4 ± 4.3	8.8 ± 4.0
Trimer anhydroMurNAc	7.0 ± 0.3	9.5 ± 1.0*	6.2 ± 1.3	10.3 ± 1.0*
Trimers (total)	15.4 ± 2.8	18.3 ± 4.0	16.2 ± 5.5	19.4 ± 1.8
Dipeptides (total)	2.1 ± 0.1	n.d.*	7.2 ± 0.5*	n.d.*
Tripeptides (total)	22.4 ± 0.6	**0.2 ± 0.3***	29.3 ± 0.5*	n.d.*
Tetrapeptides (total)	54.3 ± 1.1	79.3 ± 2.0*	41.4 ± 4.2	75.7 ± 1.4*
Pentapeptides (total)	19.0 ± 1.3	18.2 ± 0.9	19.5 ± 0.6	21.8 ± 5.0
AnhydroMurNAc (total)	13.1 ± 3.3	13.6 ± 2.6	14.9 ± 5.4	14.5 ± 3.8
Average chain length	7.9 ± 2.0	7.5 ± 1.4	7.2 ± 2.6	7.1 ± 1.9
Degree of cross-linkage	33.1 ± 0.7	35.3 ± 2.8	35.3 ± 2.2	34.3 ± 1.0
% peptides in cross-links	61.1 ± 0.5	64.4 ± 4.3	65.1 ± 2.6	62.2 ± 2.6

[1] values are mean ± variation of two biological replicates.
[2] n.d., not detected.

334

335

336 **Bd1075 structure determination**

337 The structure of mature Bd1075 protein was determined to 1.34 Å (Fig. 5 and

338 Supplementary Table 2). The Bd1075 structure contains two domains: the catalytic

339 LD-CPase domain (aa 47-180) and a C-terminal nuclear transport factor 2 (NTF2)-like

340 domain (aa 196-304) (Fig. 5a). Interestingly, although there was a global agreement

341 in fold to Csd6 of *H. pylori* and Pgp2 of *C. jejuni* which also contain an NTF2 domain

342 and an LD-CPase domain (the junction between the two at residue 188 of Bd1075),

343 there were significant differences in fold elements and local regions. These differences

344 resulted in an inability to solve Bd1075 via molecular replacement, necessitating the

345 use of SAD phasing with co-crystallized halide ions. The Bd1075 protein is monomeric

346 (the two molecules in the asymmetric unit contact one another by packing interactions

347 only), lacking the dimerization regions of the other characterized LD-CPase proteins;

348 this was supported by size exclusion data (Supplementary Fig. 11).

349 We were able to trace residues 29-308 with the exception of a presumably flexible

350 region (aa 82-91) which we term the active site "lid". Differences to other LD-CPase

351 structures are distributed throughout the fold (and in a small shift in NTF2:LD-CPase

352 juxtaposition) as demonstrated by RMSD values for the full-length/LD-CPase-

353 alone/NTF2-alone of 2.5 / 2 / 1.8 Å for Csd6 and 2.8 / 1.9 / 2.2 Å for Pgp2. The large

354 values of 2.5/2.8 Å for full-length RMSD are in contrast with the agreement of 1.8 Å

355 between Csd6 and Pgp2, hence Bd1075 is the structural outlier of the three proteins.

356 Bd1075 has a consensus active site, with the superfamily conserved catalytic triad

357 consisting of C156, H141 and A142, each present in the expected (presumed active)

358 orientations (Fig. 5b). A142 is often a glycine residue in other LD-CPases but here it

359 makes identical h-bonding contacts to H141 using backbone carbonyl atoms. Bd1075

360   active site pocket-forming residue V158 is a relative anomaly as this position is an

361   arginine in most LD-transpeptidases or an alanine in Csd6/Pgp2 and YafK-like

362   enzymes shown recently to cleave the cross-link between PG and Braun's

363   lipoprotein[31, 32]. The termini of Bd1075 are very different to both Csd6 and Pgp2,

364   replacing the N-terminal dimerization domain of those enzymes with a simple, shorter

365   loop, and extending the C-terminus such that the Bd1075 NTF2 domain finishes with

366   a longer beta-strand (aa 295-306) - residues of which contribute to its binding pocket

367   (Fig. 5d-e). The C-terminus has a further 21 residues that we were unable to fit in this

368   crystal form and which are predicted to be at least partly disordered.

369   Most noteworthy within the core of the Bd1075 C-terminus was the presence of W303

370   which is clearly located within the substrate binding pocket of the NTF2 domain. W303

371   is highly conserved amongst *Bdellovibrio* Bd1075 protein homologs but not found in

372   other LD-CPase proteins (due to their shorter NTF2 sequences which terminate at a

373   position equivalent to Bd1075^{E302}). The crystal packing of Bd1075 was such that a two

374   amino acid loop of P107/K108 from one Bd1075 monomer packed into the NTF2

375   domain of the adjacent monomer. This loop is situated in an identical position to the

376   bound glycerol of Csd6, postulated to be reminiscent of a substrate-like interaction[28].

377   Conserved residues of the Bd1075 NTF2 domain binding pocket pack around this

378   feature (yellow in Fig. 5c), the base of which is formed by Y274 – an important residue

379   in both our monomeric structure and other dimeric LD-CPases.

380   Having begun to probe the cellular localization of Bd1075 in *B. bacteriovorus,* we used

381   this new structural information to aid in the construction of fluorescently-tagged

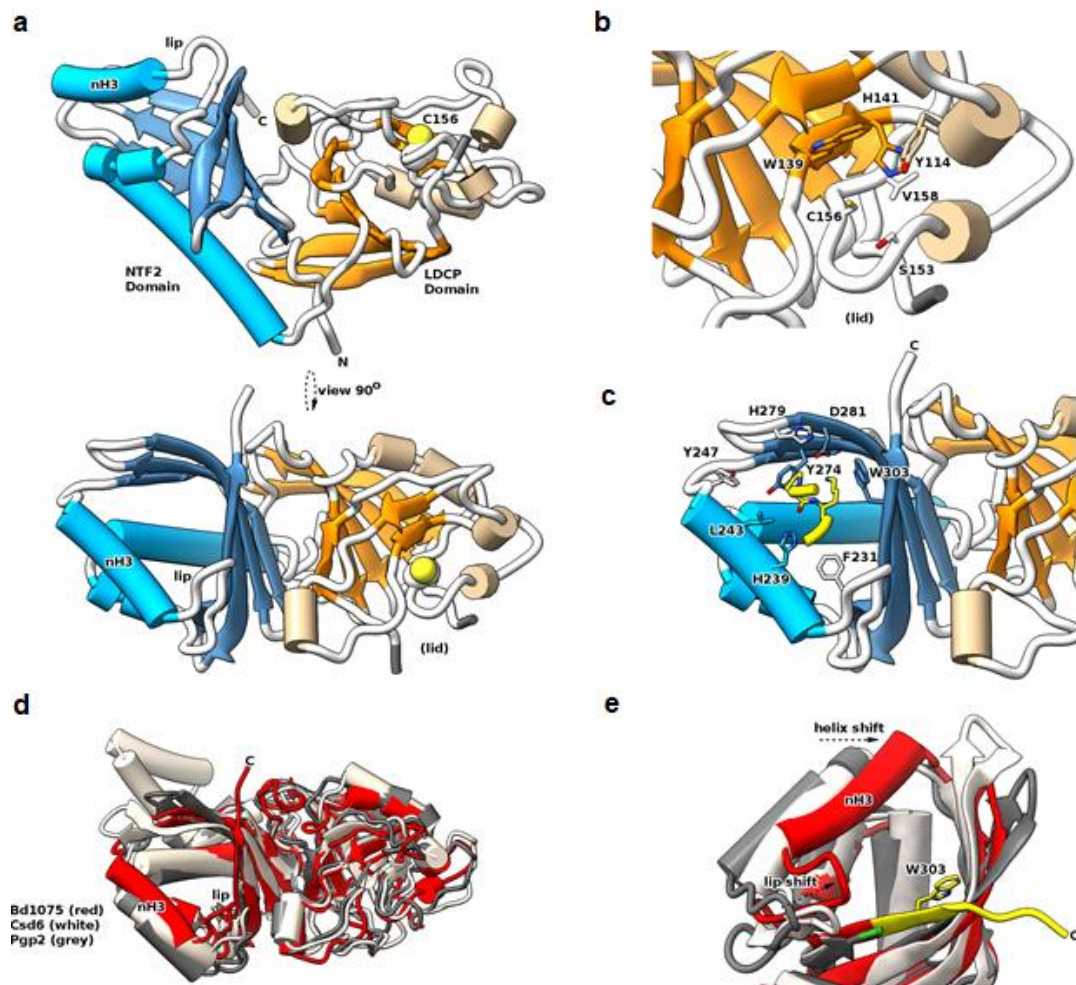382   Bd1075 truncations and point mutants for enzyme localization tests.

383

Fig 5. Structure of Bd1075 and features different to other characterized LD-CPase enzymes.

a Two orthogonal views of the Bd1075 fold, with catalytic residue C156 in space-fill form and features labeled. **b** Close-up view of the Bd1075 LD-CPase catalytic domain with selected residues that form the active site pocket displayed in stick form. **c** Close-up view of the Bd1075 NTF2 pocket, demonstrating complexation of a loop (residues 106-109 colored yellow, P107 and K108 in stick form) from a neighboring molecule in the crystal lattice. **d** Comparison of Bd1075 (red, 7O21), Csd6 (white, 4XZZ) and Pgp2 (gray, 6XJ6) structures. Helix 3 of the Bd1075 NTF2 domain (labeled "nH3") and the associated loop ("lip") are relatively closer to the NTF2 pocket than the respective features of Csd6/Pgp2. **e** Close-up of the NTF2 terminus from structural alignment in (**d**), demonstrating the relative extension of the Bd1075 C-terminus (colored yellow, includes NTF2 pocket-forming residue W303) in comparison to the shorter Csd6/Pgp2 termini (end residue colored green). The relative shifts of the nH3 helix and lip loop to constrict the NTF2 pocket are denoted by dashed arrows.

384

The C-terminal NTF2 domain of Bd1075 targets the protein to what becomes the outer convex cell face, and is required to generate curvature

Localization and targeting of Bd1075 to the outer convex cell face

To determine whether Bd1075 is broadly active over all *B. bacteriovorus* envelope PG or if activity is specifically localized, a double-crossover markerless strain in which mCherry is C-terminally fused to Bd1075 was constructed. Bd1075-mCherry localized to the outer convex face of *B. bacteriovorus* - both in free-swimming attack-phase cells (Fig. 6a) and throughout the predatory cycle (Supplementary Fig. 12). This contrasts with most characterized vibrioid cell shape-determinants in other bacteria such as *Caulobacter crescentus* and *Vibrio cholerae*, which typically localize to the inner concave face[24, 26].

Moreover, unlike pole-associated proteins, the mechanism by which bacterial proteins are targeted to one of the cell lateral sides has not been described. Intrigued and partly informed by the protein structural data, we utilized the specifically-targeted Bd1075 to investigate how bacterial proteins might be targeted to just one lateral wall. We hypothesized that, in addition to the N-terminal signal peptide which targets the protein for translocation into the periplasm, Bd1075 may contain a second internal targeting sequence which directs the protein to just one side of the periplasm: the wall that becomes the outer curve. We therefore constructed five different protein variants of Bd1075 which were each C-terminally fused to mCherry (Fig. 6b). These constructs were then introduced into the *B. bacteriovorus* HD100 curved wild-type strain to generate single-crossover strains containing two copies of *bd1075*: the original wild-

408   type and the new mCherry fusion. The sub-cellular localization of each fusion protein

409   was then examined by epifluorescence microscopy.

410   As expected, the full-length protein localized to (what becomes) the convex cell face

411   (Fig. 6c) and we noted no morphological nor deleterious effects resulting from the

412   presence of two functional copies of *bd1075*. The LD-CPase domain contains three

413   conserved catalytic triad residues: His-141, Ala-142 and Cys-156. Mutation of Cys-

414   156 to alanine (C156A) in full length Bd1075 did not abrogate localization, indicating

415   that LD-CPase activity is not involved in targeting (Fig. 6c).

416   As the Bd1075 C-terminal NTF2 domain (aa 196-304) is from a very broad protein

417   superfamily[33], it was not possible to predict a putative function for this domain but the

418   structure with the P107/K108 loop bound over the NTF2 pocket (Fig. 5c) suggested

419   that this was a substrate interaction mimic and a means to destabilize putative PG

420   substrate interactions. We tested a role for the NTF2 domain in protein targeting via

421   the generation of three additional mCherry fusions: (1) Full-length Bd1075 containing

422   an NTF2 domain point mutation changing Tyr-274 (which forms the base of the

423   substrate-binding pocket, Fig. 5c) to alanine: Y274A; (2) Bd1075 truncated protein

424   comprising residues 1-E302 (similar to the shorter Csd6 and Pgp2) which terminates

425   2 residues prior to the completion of the NTF2 domain at A304, omitting the highly

426   conserved W303 which the crystal structure had suggested to be a Bd1075-unique

427   feature; and (3) Bd1075 truncated protein comprising residues 1-A304, completing the

428   NTF2-like domain and including W303.

429   The Y274A and E302 truncated mutants (which both contain disruptions to the NTF2

430   domain) failed to localize to the outer curve, however the A304 truncation mutant

431   which contains a complete NTF2 domain (and *Bdellovibrio*-specific residue W303) was

432   correctly targeted (Fig. 6c). These results strongly supported the hypothesis that the

433   NTF2 domain is involved in protein targeting to the PG side-wall (which becomes the

434   convex cell face), and that the *Bdellovibrio*-specific NTF2 extension, including W303,

435   is important for this function.

436

The role of protein targeting in the generation of curvature

438   To investigate whether correct protein targeting is absolutely required to generate

439   curvature, the five mCherry fusion constructs were introduced into the rod-shaped

440   Δ*bd1075* mutant to generate single-crossover strains expressing solely the mCherry-

441   tagged copy of *bd1075*. The sub-cellular localization and curvature of each fusion

442   strain were examined. The full-length protein localized to (what becomes) the outer

443   curve and completely complemented the curvature of Δ*bd1075* (Fig. 6d-e). The LD-

444   CPase catalytic domain point mutant C156A did not restore curvature and remained

445   localized at the center of the rod-shaped cell (Fig. 6d-e). Critically, neither of the NTF2

446   domain mutants Y274A nor E302 were correctly targeted and neither protein could

447   complement the curvature of Δ*bd1075* (Fig 6d-e), highlighting the importance of the

448   NTF2 domain and residue W303.

449   Together, these targeting data reveal that the NTF2 domain is responsible for

450   targeting Bd1075 to the outer curve of the bacterial periplasm and that this specific

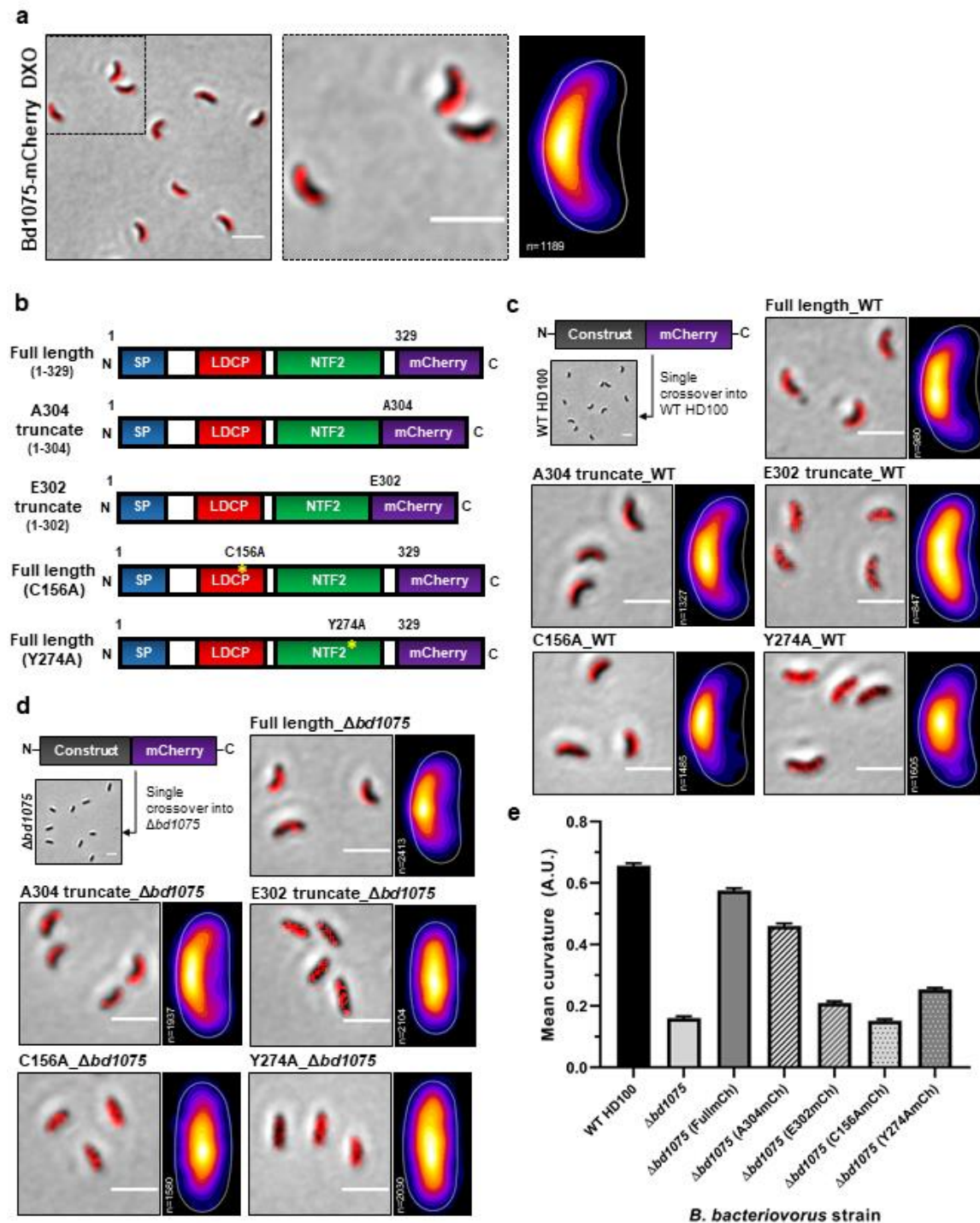451   localization is required to generate cell curvature.

452

453

454

Fig. 6 The NTF2 domain is required to target Bd1075 to what becomes the convex cell face and generate curvature at that site.

a *B. bacteriovorus* Bd1075-mCherry double-crossover (DXO) attack-phase cells (left), showing the localization of wild-type Bd1075-mCherry to the convex cell face, and representative of 3 biological repeats. Dashed boxed region is shown in a close-up (middle). Scale bars = 2 μm. Heatmap (right) depicts the location of wild-type Bd1075-mCherry foci detected in n = 1189 cells from 3 biological

repeats. White-yellow = highest intensity, purple-black = lowest intensity. **b** Schematics of Bd1075-mCherry single-crossover constructs used in (**c-e**). Full-length: Residues 1-329 (wild-type complete protein) fused to mCherry, A304: Residues 1-304 (contains a completed NTF2 domain including the *B. bacteriovorus*-specific residue W303) fused to mCherry, E302: Residues 1-302 (does not complete the NTF2 domain) fused to mCherry, C156A: Residues 1-329 (full-length with a point mutation of C156A in the catalytic LD-CPase domain) fused to mCherry, and Y274A: Residues 1-329 (full-length with a point mutation of Y274A in the NTF2 domain) fused to mCherry. **c-d** Bd1075-mCherry single-crossover constructs introduced into either *B. bacteriovorus* HD100 **c** wild-type (contains a native wild-type copy of *bd1075*) or **d** Δ*bd1075* (lacking a wild-type copy of *bd1075*). Attack-phase cell images and adjacent heatmaps show targeting of Bd1075-mCherry. Images and heatmaps were generated from 3 biological repeats (n = number of cells analyzed). Scale bars = 2 μm. **e** Curvature measurements of *B. bacteriovorus* Δ*bd1075* attack-phase cells containing different single-crossover Bd1075-mCherry fusions. n = 1886-2812 cells per strain from 3 biological repeats. Error bars represent standard error of the mean. All pairwise comparisons between strains (except for Δ*bd1075 vs* Δ*bd1075* (C156mCh) were significant (p<0.0001; Kruskal-Wallis test). Frequency distributions are included in Supplementary Fig. 5c.

455

456

457

458

459

460

461

462

463

464

Discussion

In this work, we elucidate the first vibrioid cell shape-determinant of predatory *Bdellovibrio bacteriovorus* bacteria and show that vibrioid morphology confers dual fitness benefits to predators: rapid prey invasion and optimal intracellular growth. These findings contribute to fundamental knowledge of bacterial cell shape and deepen our understanding of the predatory process, which may assist the application of predatory bacteria as a therapeutic.

In vibrioid bacteria, intermediate filament-like (IF-like) cyto- or periskeletal elements frequently determine cell shape[24, 26]. IF-like proteins often contain coiled-coil rich protein (Ccrp) domains, however deletion of the sole *B. bacteriovorus* Ccrp protein was previously found not to affect vibrioid cell shape[34]. Here, we discover that the vibrioid curvature of *B. bacteriovorus* is instead determined by a PG cell wall hydrolase: Bd1075. Refining the initial prediction of an LDT domain, we show via sacculus studies that Bd1075 functions as an LD-CPase, cleaving both cross-linked and uncross-linked tetrapeptides to tripeptides in the predator PG cell wall (Fig. 4 and Table 1). This enzymatic activity was also observed for LD-CPase helical shape-determining proteins Csd6 (*H. pylori*) and Pgp2 (*C. jejuni*), highlighting the importance of biochemical validation of predicted LDT domains.

Considering how PG hydrolytic activity generates bacterial cell curvature, it is possible that targeted LD-CPase-mediated reduction in tetrapeptides may reduce localized cross-linking by DD- or LD-transpeptidases. Consistent with this idea, the overall peptide cross-linkage was slightly higher in cells lacking *bd1075* (64.4% compared to 61.1% in wild-type, Table 1). We theorize that a reduction in PG cross-linkage could soften one side of the PG sacculus such that the cell bulges slightly and becomes

489   deformed by internal cellular turgor pressure which pushes outwards to generate an

490   outer convex curve that may be fixed by subsequent, as yet uncharacterized, enzyme

491   activity.

492   *B. bacteriovorus* vibrioid curvature is widely conserved within this group of invasive

493   predators with the exception of the rod-shaped and long-cultured laboratory strain *B.*

494   *bacteriovorus* 109J. Originally named *B. bacteriovorus* 109, the strain was re-

495   designated as 109J following the observation that, in one research laboratory, predator

496   cells had transitioned from a curved to non-vibrioid shape[35]. It is possible that long-

497   term laboratory culture conditions in which prey are highly abundant may have

498   removed the selection pressure for vibrioid morphology, resulting in the lab-evolved

499   57-residue deletion that we detect to have inactivated $Bd1075_{109J}$. $Bd1075_{109J}$ was not

500   catalytically active upon PG (Supplementary Fig. 8a, Supplementary Fig. 9b, and

501   Supplementary Table 1) and therefore could not complement curvature when cross-

502   expressed in HD100 Δ*bd1075* (Supplementary Fig. 4). Despite retaining LD-CPase

503   catalytic residues and targeting capability, the 57-residue N-terminal truncation could

504   severely disrupt $Bd1075_{109J}$ protein folding and therefore function. The mutation most

505   likely occurred via homologous recombination between 8 bp repeats which flank the

506   deleted region (Supplementary Fig. 3b); this has been observed in other predator

507   genes[36].

508   Bacterial morphology is evolutionarily conserved and known to confer selective

509   advantages to different bacterial lifestyles[37, 38]. The helical morphology of *H. pylori*, for

510   example, facilitates efficient bacterial motility through the gastric mucosa to allow

511   pathogenic colonisation of the gastrointestinal tract[19]. Moreover, rod-shaped mutants

512   of helical *C. jejuni* are deficient or have reduced fitness in a model of chick

513   colonisation[21, 22]. In *V. cholerae*, vibrioid cell curvature (which is generated via a

514   different non-enzymatic mechanism) increases motility through dense soft-agar

515   matrices and promotes the colonisation of *V. cholerae* in motility-dependent mouse

516   and rat infection models[26].

517   Here, we propose new phenotypic roles for bacterial cell curvature: invasion and

518   growth within Gram-negative prey bacteria. Straight rod-shaped *B. bacteriovorus*

519   Δ*bd1075* predators invade prey significantly more slowly than curved wild-type

520   predators (Fig. 2c). During prey invasion, *B. bacteriovorus* must presumably overcome

521   opposing physical forces exerted upon itself by the turgid prey membrane and cell

522   wall. Curved predators may distribute opposing forces as a glancing blow along the

523   predator cell body, facilitating an efficient, curved trajectory into rounded prey, in

524   contrast to force-intensive 'head-on' invasions by rod-shaped predators.

525   Unlike wild-type curved *B. bacteriovorus*, non-vibrioid Δ*bd1075* predators stretch and

526   deform the rounded prey bdelloplast (Fig. 3c-e). Intriguingly, non-vibrioid Δ*bd1075*

527   predators become gradually curved during elongation inside spherical prey

528   bdelloplasts, despite the absence of *bd1075* (Fig. 3a-b). The Δ*bd1075* predator does

529   not curve as tightly as the wild-type, however, and released progeny cells are not

530   curved but rod-shaped, indicating that adoption of an intracellular curvature is

531   temporary in this mutant (Fig. 3a). In wild-type curved predators, Bd1075 may thus be

532   acting enzymatically on the *B. bacteriovorus* PG wall to tighten and "fix" a bdelloplast-

533   imposed curve, consequently avoiding damage to the replicative niche, while also

534   preparing curved and invasively-streamlined progeny predators for prey exit. This

535   suggests a sensing and usage by predatory bacteria of the spherical prey environment

536   - possibly to localize shape-determining enzyme(s) at a topologically-imposed curve

537   ("curvature-templating") and initiate the permanent "fixation" of a vibrioid cell shape.

538   This topological-sensing could be a mechanism utilised more generally by bacteria or

539   alternatively the structural differences of Bd1075 (monomeric, C-terminal extension)

540   compared to the shape-determinants of free-living helical bacteria could render the

541   usage of "curvature-templating" predator-specific.

542   Fluorescently-tagged Bd1075 specifically localizes to (what becomes) the outer

543   convex face of vibrioid *B. bacteriovorus* cells (Fig. 6a). Most cell shape enzymes (for

544   which localization is known) are found at the inner concave face of bacteria. These

545   include the *C. crescentus* cytoskeletal polymer crescentin[24] and *Vibrio cholera*e CrvA

546   and CrvB which form periskeletal polymers[26, 39]. Only Bd1075 and the *H. pylori*

547   bactofilin CcmA have been identified at the outer convex face of bacterial cells,

548   occupying the periplasmic and cytoplasmic compartments, respectively[40].

549   To our knowledge, there is currently no known mechanistic basis for asymmetric

550   bacterial protein targeting to one lateral side-wall of the cell. Intrigued by this and

551   guided by the phenotyping of Bd1075 protein truncations and point mutations, we

552   discover that the extended C-terminal NTF2 domain (including the unique pocket

553   residue W303) targets the protein to the convex face and is necessary to generate cell

554   curvature (Fig. 6c-e). NTF2 is a nuclear envelope protein which transports molecules

555   into eukaryotic nuclei[41]. The NTF2-like domain superfamily, however, comprises

556   hundreds of thousands of proteins spanning the 3 domains of life and is associated

557   with over 200 biological pathways, suggestive of divergent evolution[33, 42].

558   The NTF2 domain of *C. jejuni* Pgp2 was recently found by NMR studies to bind a

559   variety of PG fragments, with specific secondary structure features shifting upon

560   complexation[43]. The general agreement of some of the structure of monomeric

561   Bd1075 with dimeric Pgp2 is suggestive that Bd1075 binds PG. The hydrogen-bond

562   rich nature of the P107/K108 loop we observe in our crystal structure could be

563   indicative of such an interaction by mimicking part of a PG muropeptide. Since the

564   Pgp2 study invoked an induced fit on binding PG, it is particularly interesting that the

565   third helix of the Bd1075 NTF2 domain (nH3, aa 233-248) and associated loop

566   (labeled "lip", aa 226-232) are shifted in relation to both Pgp2 and Csd6 (Fig. 5d). This

567   helix was the major NTF2 feature that was reported to shift upon Pgp2-PG binding[43].

568   We postulate that its position has been modified in our Bd1075 structure by sidechains

569   contacting the P107/K108 loop and may thus represent a "bound" state. There is also

570   the potential for NTF2:LD-CPase domain crosstalk, given that a small LD-CPase

571   domain helix (aa 125-132) shifts in response to NTF2 alterations[43], and in Bd1075

572   appears to influence the disorder of the adjacent active site lid domain.

573   Since Bd1075 localizes to one lateral side-wall, one could theorize that the PG or outer

574   membrane properties of that particular side-wall must be uniquely different to the

575   other. One possibility is that the NTF2 domain recognizes a modification or substrate

576   which is more abundant at this side-wall. Alternatively, the NTF2 domain may

577   recognize the temporary physical curvature imposed by growth inside the spherical

578   bdelloplast ("curvature-templating") and direct Bd1075 to this curved cell face. Bd1075

579   may then exert LD-CPase activity, initiating the "fixation" of *B. bacteriovorus* curvature.

580   Such a possible curvature-templating mechanism is supported by the localization of

581   Bd1075 (C156A)-mCherry in Δ*bd1075* (Fig. 6d). This construct should be capable of

582   correct asymmetric localization to one lateral side-wall (but not curvature generation),

583   however the C156A-mCherry protein remained localized to the cytoplasm of the rod-

584   shaped Δ*bd1075* attack-phase cells which have been released from bdelloplasts (Fig.

585   6d). This supports the idea that Bd1075 may sense and localize to temporary

586   curvature that is templated by the spherical bdelloplast shape. These questions -

587   which would present a significant investigative challenge beyond the scope of this

588   study - could indicate whether bacteria have evolved to sense the topology of their

589   physical space environment and use that dynamically to template their final

590   morphotype during growth and replication.

591   Collectively, these findings advance our understanding of factors affecting the fitness

592   of therapeutically-promising predatory bacteria and provide new mechanistic insights

593   into the evolutionary importance of bacterial cell morphology.

594

595

596

597

598

599

600

601

602

603

604

605

606

607

608 **Methods**

609 **Bacterial strains and culture**

610 *Bdellovibrio bacteriovorus* strains were predatorily cultured in liquid Ca/HEPES buffer

611 (5.94 g/l HEPES free acid, 0.284 g/l calcium chloride dihydrate, pH 7.6) and on solid

612 YPSC overlays, both containing *Escherichia coli* S17-1 prey as described previously[44].

613 Where appropriate, kanamycin or gentamicin were added to growth media at

614 concentrations of 50 μg ml^{-1} or 5 μg ml^{-1}, respectively.

615

616 **Plasmid and strain construction**

617 Primers and plasmids used in to construct strains used in this study are detailed in

618 Supplementary Table 3 and Supplementary Table 4. Strains are listed in

619 Supplementary Table 5. Bd1075 protein residue numbering was updated to correct for

620 a previously mis-annotated start codon; the probable true start begins 2 codons

621 downstream from that originally predicted (Supplementary Fig. 1b). To construct a

622 markerless deletion of *bd1075*, 1 kb of upstream and downstream DNA were cloned

623 into the suicide vector pK18*mobsacB* by Gibson assembly[45] using the NEBuilder HiFi

624 DNA Assembly Cloning Kit (New England Biolabs). The vector was introduced into *B.*

625 *bacteriovorus* via an *E. coli* S17-1 conjugal donor strain and a double-crossover

626 deletion mutant was isolated by sucrose suicide counter-selection as described

627 previously[8, 46]. Deletion of *bd1075* was verified by RT-PCR, Sanger sequencing and

628 whole-genome sequencing.

629 Strains for complementation tests were constructed by inserting the *bd1075* gene from

630 either strain HD100 or strain 109J (gene ID: EP01_15440) plus the respective native

631 gene promoter into the vector pMQBAD, a derivative of pMQ414 which expresses the

632 fluorescent tdTomato protein and is capable of autonomous replication in *B.*

633 *bacteriovorus*[47]. Constructs for complementation tests were verified by Sanger

634 sequencing, conjugated into *B. bacteriovorus* and maintained under a gentamicin

635 selection pressure.

636 To initially fluorescently-tag Bd1075, the stop codon of *bd1075* was replaced with the

637 *mCherry* coding sequence to generate an in-frame C-terminal fusion terminating at the

638 stop codon of the mCherry protein. The fluorescent strain was constructed and verified

639 analogously to the Δ*bd1075* mutant to generate a markerless double-crossover

640 Bd1075-mCherry strain. For more extensive analysis of domain functions, single-

641 crossover mCherry fusions to either full length or truncated versions of Bd1075 were

642 made. These were constructed by cloning 1 kb of upstream DNA, the DNA encoding

643 each desired Bd1075 domain-test (minus the stop codon) and the *mCherry* sequence

644 into pK18*mobsacB*. Point mutations in such constructs were generated using

645 Q5® Site-Directed Mutagenesis (New England Biolabs). Each construct was then

646 conjugated into *B. bacteriovorus* to generate single-crossover merodiploid strains

647 which were confirmed by Sanger sequencing and maintained under a kanamycin

648 selection pressure.

649

650 **Protein expression and purification**

651 The *bd1075* gene from *B. bacteriovorus* HD100, minus the signal peptide and stop

652 codon, was cloned into the vector pET41 in-frame with a C-terminal histidine tag and

653 transformed into *E. coli* BL21. *E. coli* BL21 was cultured in TB media and incubated at

654 37 °C with orbital shaking at 200 rpm to an OD_{600} of 0.6-0.8. *bd1075* expression was

655 then induced with 0.5 mM IPTG at 18 °C for 16 h. Bd1075 was purified to near

656 homogeneity using Ni-NTA affinity and size-exclusion chromatography, then dialyzed

657 into either buffer containing 10 mM Na Citrate pH 6.0, 30 mM KCl, and 2% w/v glycerol

658   (activity assays) or buffer containing 20 mM Na Citrate pH 6.0, 200 mM NaCl and 2

659   mM β-mercaptoethanol (structure studies).

660

661   **Muropeptide analysis**

662   To culture *B. bacteriovorus* for sacculi isolation, 1 l of each *B. bacteriovorus* strain was

663   grown on either *E. coli* S17-1 or *E. coli* S17-1 pUC19 (gentamicin-resistant prey for

664   complementation test strains containing the pMQBAD plasmid). Following complete

665   predatory lysis of *E. coli* prey during a 24 h incubation at 29 °C with orbital shaking at

666   200 rpm, *B. bacteriovorus* attack-phase cultures were passed through a 0.45 μm filter

667   to remove any remaining prey debris. To culture *E. coli* BW25113 for sacculi isolation,

668   *E. coli* was grown at 37 °C for 16 h with orbital shaking at 200 rpm. Cultured *B.*

669   *bacteriovorus* or *E. coli* cells were then centrifuged at 15,000 g for 30 min at 4 °C,

670   resuspended in 6 ml of ice-cold PBS, and then boiled in 6 ml of 8% SDS for 30 min to

671   lyse the cells and liberate sacculi. Peptidoglycan was purified from the cell lysates,

672   then muropeptides in the supernatant were reduced with sodium borohydride and

673   HPLC analysis performed as previously described[48].

674

675   To test the *in vitro* activity of Bd1075$_{HD100}$, sacculi from either *B. bacteriovorus* HD100

676   Δ*bd1075*, *B. bacteriovorus* wild-type 109J or *E. coli* BW25113 were incubated with 10

677   μM of *B. bacteriovorus* Bd1075$_{HD100}$ in 50 mM Tris-HCl, 50 mM NaCl, pH 7.0 for 16 h

678   at 37 °C on a thermomixer at 900 rpm. The control sample received no enzyme. To

679   stop Bd1075 activity, the samples were boiled at 100 °C for 10 min and an equal

680   volume of 80 mM sodium phosphate, pH 4.8, was added. The samples were incubated

681   with 10 μg of cellosyl (Hoechst, Frankfurt am Main, Germany) for a further 16 h at 37

682   °C on a thermomixer at 900 rpm, boiled for 10 min and centrifuged at room

683   temperature for 15 min at 16,000 g. Muropeptides present in the supernatant were

684   reduced with sodium borohydride and analyzed by HPLC as described[48].

685

686   **Structure determination**

687   Purified Bd1075 at ~25 mg/ml was used for screening. Crystals were grown at 18 °C

688   using the sitting drop technique in 4 µl drops composed of equal volumes of protein

689   and reservoir solution. B1075 crystals were obtained in the BCS™ screen (Molecular

690   Dimensions) in condition 2-44, comprising 0.1 M Tris pH 7.8, 0.1 M KSCN, 0.1 M NaBr

691   and 25% PEG Smear broad range. Crystals were cryo-protected in mother liquor

692   supplemented with 25% (v/v) ethylene glycol and flash cooled in liquid nitrogen.

693   Diffraction data were collected at the Diamond Light Source in Oxford, UK

694   (Supplementary Table 2). Data reduction and processing were completed using XDS[49]

695   and the xia2 suite[50]. Bd1075 phasing was achieved using a merged SAD data set

696   (9000 frames, 0.1° oscillations) collected at a wavelength of 0.91 Å corresponding to

697   the bromide anomalous scattering peak. The collected data were input into CCP4

698   online CRANK2[51], which located six bromide sites with an initial FOM of 0.14, followed

699   by iterative cycles of building and model-based phasing improvement. The obtained

700   model was further built and modified using COOT[52], with cycles of refinement in

701   PHENIX[53].

702

703   **Phase-contrast and epifluorescence microscopy**

704   *B. bacteriovorus* cells were immobilized on a thin 1% Ca/HEPES buffer agarose pad

705   and visualized under a Nikon Ti-E inverted epifluorescence microscope equipped with

706   a Plan Apo 100x Ph3 oil objective lens (NA: 1.45), an mCherry filter (excitation: 555

707　nm, emission: 610-665 nm), and an mCerulean3 filter (excitation: 440 nm, emission:

708　470-490 nm). Images were acquired on an Andor Neo sCMOS camera with Nikon NIS

709　software. Images were analyzed using the Fiji distribution of ImageJ[54] and minimally

710　processed using the sharpen and smooth tools, with adjustments to brightness and

711　contrast. The MicrobeJ plug-in for ImageJ[55] was used to measure cell morphologies

712　and detect fluorescent foci. *B. bacteriovorus* attack-phase cells were generally

713　identified by the parameters of area: 0.2-1.5 μm^2, length: 0.5-2.5 μm, width: 0.2-0.8

714　μm, and circularity: 0-0.9 A.U. For the detection of Bd1075-mCherry fluorescent

715　fusions in a curved wild-type genetic background, *B. bacteriovorus* cells were defined

716　with the same parameters, but excluded cells with a curvature of <0.6 so as to only

717　measure localization in cells with a definitively curved shape. Curvature parameters

718　were set to 0-max to allow measurements of curvature for fluorescent fusions

719　expressed in a non-curved Δ*bd1075* genetic background. Fluorescent Bd1075-

720　mCherry foci within attack-phase *B. bacteriovorus* cells were detected with the foci

721　method using default maxima settings and an association with parent bacteria with a

722　tolerance of 0.1 μm. Images were manually inspected to ensure cells had been

723　correctly detected before measurements were acquired. To analyze prey bdelloplast

724　morphology, bdelloplasts were generally identified by the parameters of area: 1.0-max

725　μm^2, length: 0.5-max μm, width: 0.5-max μm, and circularity: 0.8-max A.U. *B.*

726　*bacteriovorus* cells were detected in the maxima channel with the bacteria method

727　using default maxima settings and an association with parent bacteria with a tolerance

728　of 0.1 μm. Only the morphologies of prey bdelloplasts which contained a single *B.*

729　*bacteriovorus* predator were measured.

730

731　**Electron microscopy**

732   *B. bacteriovorus* cells were cultured for 24 h, then concentrated by microcentrifugation

733   at 5,000 g for 10 min followed by careful resuspension in 1 ml of Ca/HEPES. *B.*

734   *bacteriovorus* cells were applied to glow-discharged Formvar/Carbon-coated 200-

735   mesh copper grids (EM Resolutions), stained with 0.5% uranyl acetate for 1 min, then

736   de-stained with Tris-EDTA pH 7.6 for 30 s. Samples were imaged under a FEI Tecnai

737   G2 12 Biotwin transmission electron microscope at 100 kV.

738

739   **Time-lapse microscopy**

740   For time-lapse microscopy, 1 ml cultures of attack-phase *B. bacteriovorus* and 50 µl

741   of stationary-phase *E. coli* S17-1 were microcentrifuged separately at 17,000 g for 2

742   min, then resuspended in 50 µl of Ca/HEPES. Predators and prey were then mixed

743   together and immediately transferred to a thin 0.3% Ca/HEPES agarose pad. Cells

744   were visualized under a Nikon Eclipse E600 upright microscope equipped with a 100x

745   oil objective lens (NA: 1.25) and a Prior Scientific H101A XYZ stage which allowed 6

746   specific fields of view to be revisited over the time-lapse sequence. Image frames were

747   captured every 1 min for at least 2 h on a Hammamatsu Orca ER Camera with Simple

748   PCI software. Time-lapse videos of *B. bacteriovorus* attaching to and entering *E. coli*

749   prey were analyzed in Simple PCI software. Attachment time was measured by

750   counting the number of frames (1 frame = 1 min) between initial irreversible predator

751   attachment to prey and the first indication of the predator moving into prey. Entry time

752   was measured by counting the number of frames between the first indication of the

753   predator moving into prey and the predator residing completely inside the bdelloplast.

754

755

756   **Statistical analysis**

757   Statistical analysis was performed in Prism 8.0 (GraphPad). Data were first tested for

758   normality and then analyzed using an appropriate statistical test. The number of

759   biological repeats carried out, n values for cell numbers, and the statistical test applied

760   to the data set are described in each figure legend.

761

762   **Data availability**

763   Coordinates and structure factors have been deposited in the PDB under the accession

764   code 7O21.

765   **Acknowledgements**

776   **Author contributions**

777   E.J.B. made all deletion, complementation and fluorescent strains of Bd1075, carried out

778   curvature analysis and conducted electron, time-lapse, and epifluorescence microscopy

779   experiments with supervision by R.E.S. and C.L. J.B. carried out PG sacculi purifications and

780   HPLC analysis with supervision by W.V. I.T.C. made the *bd1075* expression construct for

781   protein purification. A.W purified the protein with purification optimization and protocol design

782   from I.T.C. M.V-D crystallized and solved the structure of Bd1075. All protein work was

783 supervised by A.L.L. E.J.B., R.E.S. and A.L.L. wrote the manuscript and all co-authors read

784 and approved the final manuscript.

785 **Competing interests**

786 The authors declare no competing interests.

787 **Additional information**

788 **Supplementary information** is available at [X]

789 **Correspondence** and requests for materials should be addressed to R.E.S.

790

791

792

793

794

795
796
797
798
799
800
801
802
803
804
805
806
807
808
809
810
811
812
813
814
815
816

References

1. Stolp H, Starr MP. *Bdellovibrio bacteriovorus* gen. et sp. n., a predatory, ectoparasitic, and bacteriolytic microorganism. *Antonie Van Leeuwenhoek* **29**, 217-248 (1963).

2. Dashiff A, Junka RA, Libera M, Kadouri DE. Predation of human pathogens by the predatory bacteria *Micavibrio aeruginosavorus* and *Bdellovibrio bacteriovorus*. *J. Appl. Microbiol.* **110**, 431-444 (2011).

3. Kadouri DE, To K, Shanks RM, Doi Y. Predatory bacteria: a potential ally against multidrug-resistant Gram-negative pathogens. *PLoS One* **8**, e63397 (2013).

4. Atterbury RJ*, et al.* Effects of orally administered *Bdellovibrio bacteriovorus* on the well-being and *Salmonella* colonization of young chicks. *Appl Environ Microbiol* **77**, 5794-5803 (2011).

5. Shatzkes K*, et al.* Predatory bacteria attenuate *Klebsiella pneumoniae* burden in rat lungs. *MBio* **7**, (2016).

6. Willis AR*, et al.* Injections of predatory bacteria work alongside host immune cells to treat *Shigella* infection in zebrafish larvae. *Curr. Biol.* **26**, 3343-3351 (2016).

7. Silhavy TJ, Kahne D, Walker S. The bacterial cell envelope. *Cold Spring Harb. Perspect. Biol.* **2**, a000414 (2010).

8. Lerner TR*, et al.* Specialized peptidoglycan hydrolases sculpt the intra-bacterial niche of predatory *Bdellovibrio* and increase population fitness. *PLoS Pathog.* **8**, e1002524 (2012).

9. Lambert C*, et al.* Interrupting peptidoglycan deacetylation during *Bdellovibrio* predator-prey interaction prevents ultimate destruction of prey wall, liberating bacterial-ghosts. *Sci. Rep.* **6**, 26010 (2016).

10. Kuru E*, et al.* Fluorescent D-amino-acids reveal bi-cellular cell wall modifications important for *Bdellovibrio bacteriovorus* predation. *Nat Microbiol* **2**, 1648-1657 (2017).

11. Harding CJ*, et al.* A lysozyme with altered substrate specificity facilitates prey cell exit by the periplasmic predator *Bdellovibrio bacteriovorus*. *Nat Commun* **11**, 4817 (2020).

12. Shilo M. Morphological and physiological aspects of the interaction of *Bdellovibrio* with host bacteria. *Curr Top Microbiol Immunol* **50**, 174-204 (1969).

13. Lambert C, Fenton AK, Hobley L, Sockett RE. Predatory *Bdellovibrio* bacteria use gliding motility to scout for prey on surfaces. *J. Bacteriol.* **193**, 3139-3141 (2011).

864
865 14. Matin A, Rittenberg SC. Kinetics of deoxyribonucleic acid destruction and synthesis
866   during growth of *Bdellovibrio bacteriovorus* strain 109D on *Pseudomonas putida* and
867   *Escherichia coli*. *J. Bacteriol.* **111**, 664-673 (1972).
868
869 15. Hespell RB, Miozzari GF, Rittenberg SC. Ribonucleic acid destruction and synthesis
870   during intraperiplasmic growth of *Bdellovibrio bacteriovorus*. *J. Bacteriol.* **123**, 481-
871   491 (1975).
872
873 16. Ruby EG, McCabe JB, Barke JI. Uptake of intact nucleoside monophosphates by
874   *Bdellovibrio bacteriovorus* 109J. *J. Bacteriol.* **163**, 1087-1094 (1985).
875
876 17. Wyckoff TJ, Taylor JA, Salama NR. Beyond growth: novel functions for bacterial cell
877   wall hydrolases. *Trends Microbiol.* **20**, 540-547 (2012).
878
879 18. Sycuro LK*, et al.* Flow cytometry-based enrichment for cell shape mutants identifies
880   multiple genes that influence *Helicobacter pylori* morphology. *Mol. Microbiol.* **90**, 869-
881   883 (2013).
882
883 19. Sycuro LK*, et al.* Peptidoglycan crosslinking relaxation promotes *Helicobacter pylori's*
884   helical shape and stomach colonization. *Cell* **141**, 822-833 (2010).
885
886 20. Sycuro LK*, et al.* Multiple peptidoglycan modification networks modulate *Helicobacter
887   pylori*'s cell shape, motility, and colonization potential. *PLoS Pathog.* **8**, e1002603
888   (2012).
889
890 21. Frirdich E*, et al.* Peptidoglycan LD-carboxypeptidase Pgp2 influences *Campylobacter
891   jejuni* helical cell shape and pathogenic properties and provides the substrate for the
892   DL-carboxypeptidase Pgp1. *J. Biol. Chem.* **289**, 8007-8018 (2014).
893
894 22. Frirdich E*, et al.* Peptidoglycan-modifying enzyme Pgp1 is required for helical cell
895   shape and pathogenicity traits in *Campylobacter jejuni*. *PLoS Pathog.* **8**, e1002602
896   (2012).
897
898 23. Min K*, et al.* Peptidoglycan reshaping by a noncanonical peptidase for helical cell
899   shape in *Campylobacter jejuni*. *Nat Commun* **11**, 458 (2020).
900
901 24. Ausmees N, Kuhn JR, Jacobs-Wagner C. The bacterial cytoskeleton: an intermediate
902   filament-like function in cell shape. *Cell* **115**, 705-713 (2003).
903
904 25. Cabeen MT*, et al.* Bacterial cell curvature through mechanical control of cell growth.
905   *EMBO J.* **28**, 1208-1219 (2009).
906
907 26. Bartlett TM*, et al.* A periplasmic polymer curves *Vibrio cholerae* and promotes
908   pathogenesis. *Cell* **168**, 172-185 e115 (2017).
909

910 27. Almagro Armenteros JJ, *et al.* SignalP 5.0 improves signal peptide predictions using
911   deep neural networks. *Nat. Biotechnol.* **37**, 420-423 (2019).

913 28. Kim HS, *et al.* The cell shape-determining Csd6 protein from *Helicobacter pylori*
914   constitutes a new family of L,D-carboxypeptidase. *J. Biol. Chem.* **290**, 25103-25117
915   (2015).

917 29. Raghunathan D, *et al.* Engulfment, persistence and fate of *Bdellovibrio bacteriovorus*
918   predators inside human phagocytic cells informs their future therapeutic potential.
919   *Sci. Rep.* **9**, 4293 (2019).

921 30. Vollmer W, Joris B, Charlier P, Foster S. Bacterial peptidoglycan (murein)
922   hydrolases. *FEMS Microbiol. Rev.* **32**, 259-286 (2008).

924 31. Bahadur R, Chodisetti PK, Reddy M. Cleavage of Braun's lipoprotein Lpp from the
925   bacterial peptidoglycan by a paralog of l,d-transpeptidases, LdtF. *Proc. Natl. Acad.*
926   *Sci. U. S. A.* **118**, (2021).

928 32. Winkle M, *et al.* DpaA detaches Braun's lipoprotein from peptidoglycan. *MBio* **12**,
929   (2021).

931 33. Eberhardt RY, *et al.* Filling out the structural map of the NTF2-like superfamily. *BMC*
932   *Bioinformatics* **14**, 327 (2013).

934 34. Fenton AK, Hobley L, Butan C, Subramaniam S, Sockett RE. A coiled-coil-repeat
935   protein 'Ccrp' in *Bdellovibrio bacteriovorus* prevents cellular indentation, but is not
936   essential for vibroid cell morphology. *FEMS Microbiol. Lett.* **313**, 89-95 (2010).

938 35. Rittenberg SC. Nonidentity of *Bdellovibrio bacteriovorus* strains 109D and 109J. *J.*
939   *Bacteriol.* **109**, 432-433 (1972).

941 36. Cotter TW, Thomashow MF. Identification of a *Bdellovibrio bacteriovorus* genetic
942   locus, *hit*, associated with the host-independent phenotype. *J. Bacteriol.* **174**, 6018-
943   6024 (1992).

945 37. Young KD. The selective value of bacterial shape. *Microbiol Mol Biol Rev* **70**, 660-
946   703 (2006).

948 38. Yang DC, Blair KM, Salama NR. Staying in shape: the impact of cell shape on
949   bacterial survival in diverse environments. *Microbiol Mol Biol Rev* **80**, 187-203
950   (2016).

952 39. Martin NR, Blackman E, Bratton BP, Bartlett TM, Gitai Z. The evolution of bacterial
953   shape complexity by a curvature-inducing module. *bioRxiv*
954   https://doi.org/10.1101/2020.02.20.954503, (2020).

956 40. Taylor JA*, et al.* Distinct cytoskeletal proteins define zones of enhanced cell wall
957   synthesis in *Helicobacter pylori*. *elife* **9**, (2020).

959 41. Corbett AH, Silver PA. The NTF2 gene encodes an essential, highly conserved
960   protein that functions in nuclear transport *in vivo*. *J. Biol. Chem.* **271**, 18477-18484
961   (1996).

963 42. Mitchell AL*, et al.* InterPro in 2019: improving coverage, classification and access to
964   protein sequence annotations. *Nucleic Acids Res.* **47**, D351-D360 (2019).

966 43. Sheng-Huei Lin C*, et al.* Peptidoglycan binding by a pocket on the accessory NTF2-
967   domain of Pgp2 directs helical cell shape of *Campylobacter jejuni. J. Biol. Chem.*,
968   100528 (2021).

970 44. Lambert C, Sockett RE. Laboratory maintenance of *Bdellovibrio. Curr. Protoc.*
971   *Microbiol.* **Chapter 7**, Unit 7B 2 (2008).

973 45. Gibson DG, Young L, Chuang RY, Venter JC, Hutchison CA, 3rd, Smith HO.
974   Enzymatic assembly of DNA molecules up to several hundred kilobases. *Nat.*
975   *Methods* **6**, 343-345 (2009).

977 46. Lambert C, Sockett RE. Nucleases in *Bdellovibrio bacteriovorus* contribute towards
978   efficient self-biofilm formation and eradication of preformed prey biofilms. *FEMS*
979   *Microbiol. Lett.* **340**, 109-116 (2013).

981 47. Mukherjee S, Brothers KM, Shanks RMQ, Kadouri DE. Visualizing *Bdellovibrio*
982   *bacteriovorus* by using the tdTomato fluorescent protein. *Appl Environ Microbiol* **82**,
983   1653-1661 (2015).

985 48. Glauner B. Separation and quantification of muropeptides with high-performance
986   liquid chromatography. *Anal. Biochem.* **172**, 451-464 (1988).

988 49. Kabsch W. XDS. *Acta Crystallogr. D Biol. Crystallogr.* **66**, 125-132 (2010).

990 50. Winter G. xia2: an expert system for macromolecular crystallography data reduction.
991   *Journal of Applied Crystallography* **43**, 186-190 (2010).

993 51. Skubak P, Pannu NS. Automatic protein structure solution from weak X-ray data. *Nat*
994   *Commun* **4**, 2777 (2013).

996 52. Emsley P, Cowtan K. Coot: model-building tools for molecular graphics. *Acta*
997   *Crystallogr. D Biol. Crystallogr.* **60**, 2126-2132 (2004).

999 53. Zwart PH*, et al.* Automated structure solution with the PHENIX suite. *Methods Mol.*
1000   *Biol.* **426**, 419-435 (2008).

1001

1002   54.   Schindelin J*, et al.* Fiji: an open-source platform for biological-image analysis. *Nat.*
1003   *Methods* **9**, 676-682 (2012).

1004
1005   55.   Ducret A, Quardokus EM, Brun YV. MicrobeJ, a tool for high throughput bacterial cell
1006   detection and quantitative analysis. *Nat Microbiol* **1**, 16077 (2016).

1007

1008